New Results on the Onset of a Coronal Mass Ejection from 5303 Å Emission Line Observations with VELC/ADITYA-L1

R. Ramesh ⬤, V. Muthu Priyal ⬤, Jagdev Singh ⬤, K. Sasikumar Raja ⬤, P. Savarimuthu, and Priya Gavshinde
Indian Institute of Astrophysics, Koramangala 2nd Block, Bangalore 560034, Karnataka, India

Abstract

We report on the onset of a coronal mass ejection (CME) using spectroscopic observations in the 5303 Å coronal emission line with the Visible Emission Line Coronagraph (VELC) onboard ADITYA-L1, the recently launched first Indian space solar mission. The CME was observed on 2024 July 16 in association with an X1.9 class soft X-ray flare from heliographic location S05W85. The VELC observations were near the west limb of the Sun during the CME. The results obtained helped to constrain the onset time of the CME. In addition, they indicate a $\approx 50\%$ decrease in the coronal intensity near the source region of the CME due to mass depletion, a $\approx 15\%$ enhancement in the emission line width, and a redshifted Doppler velocity of about $\approx 10\,\mathrm{km\,s^{-1}}$. The nonthermal velocity associated with the line broadening is $\approx 24.87\,\mathrm{km\,s^{-1}}$.

Unified Astronomy Thesaurus concepts: The Sun (1693); Solar corona (1483); Solar coronal mass ejections (310); Solar activity (1475); Solar coronal lines (2038)

1. Introduction

The green line (5303 Å) is the brightest of all solar coronal emission lines in the visible spectral range. It is a forbidden line in the coronal spectrum and caused by the transition between the ground state fine structure levels of Fe XIV. The emission peaks at a temperature of $\approx 1.8 \times 10^6$ K. The 5303 Å line is a useful tracer of solar activity and loops in the corona. Observations of the solar corona in the 5303 Å emission line with ground-based coronagraphs have been known for several decades (J. W. Evans 1957; F. Q. Orrall & H. J. Smith 1961; A. Bruzek & H. L. Demastus 1970; H. L. Demastus et al. 1973; T. Tsubaki 1975; J. Sykora 1992; M. Guhathakurta et al. 1993; K. Ichimoto et al. 1995a; T. Sakurai 1998; J. Singh et al. 1999; L. G. Bagala et al. 2001; J. Singh et al. 2004, 2011a). The Upgraded Coronal Multi-channel Polarimeter (UCoMP; E. Landi et al. 2016), commissioned recently at the Mauna Loa Solar Observatory, is capable of observing several emission lines in the range 5303–10830 Å. Observations in the 5303 Å line from space with the Large Angle Spectrometric Coronagraph C1 (LASCO-C1; G. E. Brueckner et al. 1995) onboard Solar and Heliospheric Observatory (SOHO) have been reported by B. Inhester & R. Schwenn (1997), R. Schwenn et al. (1997), and M. Mierla et al. (2008). There are also several observations in the green line during the total solar eclipses (S. Koutchmy et al. 1983; V. Rušin et al. 1994; K. Ichimoto et al. 1995b; J. M. Pasachoff et al. 2002; M. Minarovjech et al. 2003; J. M. Pasachoff et al. 2009; J. Singh et al. 2011a; A. G. Voulgaris et al. 2012; A. Caspi et al. 2020; G. D. Muro et al. 2023). But reports of dynamic events, particularly related to coronal mass ejections (CMEs), are rare (K. P. Dere et al. 1997; S. P. Plunkett et al. 1997; K. Hori et al. 2005; I. Suzuki et al. 2006). Such observations are important to understand the thermodynamic changes in the near-Sun corona due to CMEs and other solar eruptions as

shown by B. Boe et al. (2020) using total solar eclipse data obtained from multiple sites. N. Alzate et al. (2017) showed the presence of atypical large-scale structures in coronal images obtained from two successive eclipse observations in two successive years. In both cases, the shapes of the structures were similar to that of the CME shock fronts that propagated through the same region of the corona a few hours prior to the eclipse observations. In one case, the atypical structure was dominated by cool chromospheric material. These limited studies are primarily due to the unfortunate loss of SOHO/LASCO-C1 in 1998, and practical difficulties in the observations of solar corona with ground-based coronagraphs. In this Letter, we present comprehensive measurements of the intensity, width, and Doppler shift of the 5303 Å emission line before, during, and after a CME using spectroscopic observations with Visible Emission Line Coronagraph (VELC)/ADITYA-L1.

2. The Instrument

The VELC payload onboard ADITYA-L1 is an internally occulted solar coronagraph capable of carrying out simultaneous imaging (5000 Å) and spectroscopy (5303, 7892, and 10747 Å) observations from close to the limb $r = 1.05\,R_\odot$. The 10747 Å channel can be operated in either spectroscopy or spectropolarimetry mode. The field-of-view (FOV) for the imaging channel (continuum) is 1.05–3.0 $R_\odot$. The FOV for the spectral channels is 1.05–1.5 $R_\odot$. The spectroscopic observations are carried out using four slits simultaneously. The continuum and spectroscopic channels have independent narrowband filters (NBFs). This helps to avoid overlap of spectra from the different slits in the case of spectral observations. Figure 1 shows the optical layout of VELC (B. R. Prasad et al. 2017; J. Singh et al. 2019). Sunlight enters the payload via the entrance aperture. The primary mirror forms the image of the solar disk and corona on the secondary mirror. Solar disk light and coronal light until $r = 1.05\,R_\odot$ pass through the central hole of the secondary mirror and are reflected out of the payload by the tertiary mirror. Coronal light in the range
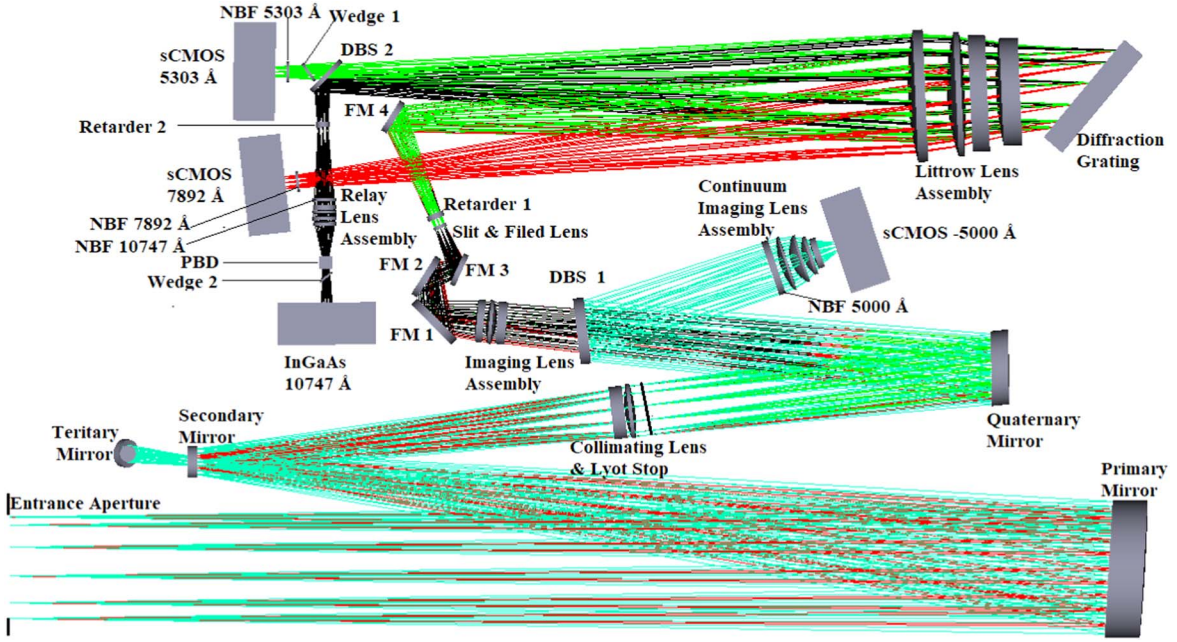
Figure 1. Optical layout of VELC.

$r = 1.05$–$3.0 \, R_\odot$ is reflected by the annular region of the secondary mirror toward the quaternary mirror, which, in turn, reflects the light toward the dichroic beamsplitter 1 (DBS1). The latter reflects the light at wavelengths $<5100 \, \text{Å}$ toward the continuum imaging lens assembly and NBF to form an image of the corona in continuum radiation at the CMOS detector. The transmitted light by DBS1 at wavelengths $>5100 \, \text{Å}$ passes through the imaging lens assembly. Then it is reflected by the mirrors FM1 & FM2 mounted on a linear scan mechanism (LSM), FM3, and forms an image of the corona on the four slits of the grating spectrograph. DBS2 separates the light at wavelengths 10747 and 5303 Å.

Figure 2 shows the four slits in the spectral channel of VELC, and their FOV at the "home" position of the LSM. The length of each slit is along the north–south direction of the Sun, and the width (dispersion) is along the east–west direction of the Sun. Some of the parameters related to the spectral channels are listed in Table 1. The observations can be carried out in either sit-and-stare mode or raster scan mode. In the case of sit-and-stare mode, fixed locations in the corona are observed by the four slits, as shown in Figure 2. Four spectra can be obtained at the same time. In raster scan mode the LSM is moved in steps at chosen time intervals to obtain an image of the corona by combining data obtained with the four slits. A distance range of $\pm 0.375 \, R_\odot$ (w.r.t the abovementioned "home" position) in the east–west direction of the coronal image can be observed using each slit by moving the LSM. All position angles (θ, measured counterclockwise from north through east) in the range $0°$–$360°$ will be covered by the four slits together. The combination of Littrow lens, grating, and narrowband filters helps to record the spectra in three emission lines (5303, 7892, and 10747 Å) simultaneously using three different detectors. The spectra recorded are analyzed to derive the parameters of the emission line such as intensity, width, and Doppler velocity at the respective locations of the corona observed. The temporal variations of the abovementioned parameters at a particular spatial location can be studied using sit-and-stare observations. Their spatial variation, either over a larger area in the corona or the entire corona within the FOV, can be studied using raster scan observations. More details of the VELC payload can be found in J. Singh et al. (2011b), B. R. Prasad et al. (2017), S. N. Venkata et al. (2017), N. Raj Kumar et al. (2018), J. Singh et al. (2019), N. Suresh Venkata & B. R. Prasad (2021), B. R. Prasad et al. (2023), J. Singh et al. (2024), M. Priyal et al. (2024), and S. Mishra et al. (2024).

3. Observations and Data Analysis

The observations reported were carried out with VELC/ ADITYA-L1 in its 5303 Å channel. Due to various technical issues, useful data were available in this channel only. The observational parameters related to the present work are listed in Table 2. For the sit-and-stare mode, the LSM was positioned such that the center of slit 4 observes the corona at $r = 1.05 \, R_\odot$ in the west direction of the Sun. In total, 703 spectra were recorded. Each spectrum was corrected for dark current, curvature of the spectra, flat field, and background. After the corrections, the emission line profile for each spatial location along the slit was generated. Then the emission line profile was fitted with a Gaussian to compute the peak intensity, width of the emission line, and Doppler velocity at each spatial location along the slit. The average central position of the emission line for the background corona was used as a reference to compute the Doppler velocity. All of the 703 spectra were analyzed similarly to derive the abovementioned emission line parameters as a function of time, and spatial locations along the slit. The computed emission parameters for each spectrum along the spatial direction in the FOV were stacked as a function of time. The image shown in Figure 3 was constructed using the peak intensity of the emission line. The x-axis in the image corresponds to Universal Time (UT). The y-axis is the spatial extent of slit 4 corresponding to the position angle range $\approx 250°$–$290°$. Note that the heliocentric distances of the coronal regions at position angles $250°$ and $290°$ are $r \approx 1.12 \, R_\odot$ as compared to $r = 1.05 \, R_\odot$ for the center of slit 4. This is due to the straight nature of the slit.
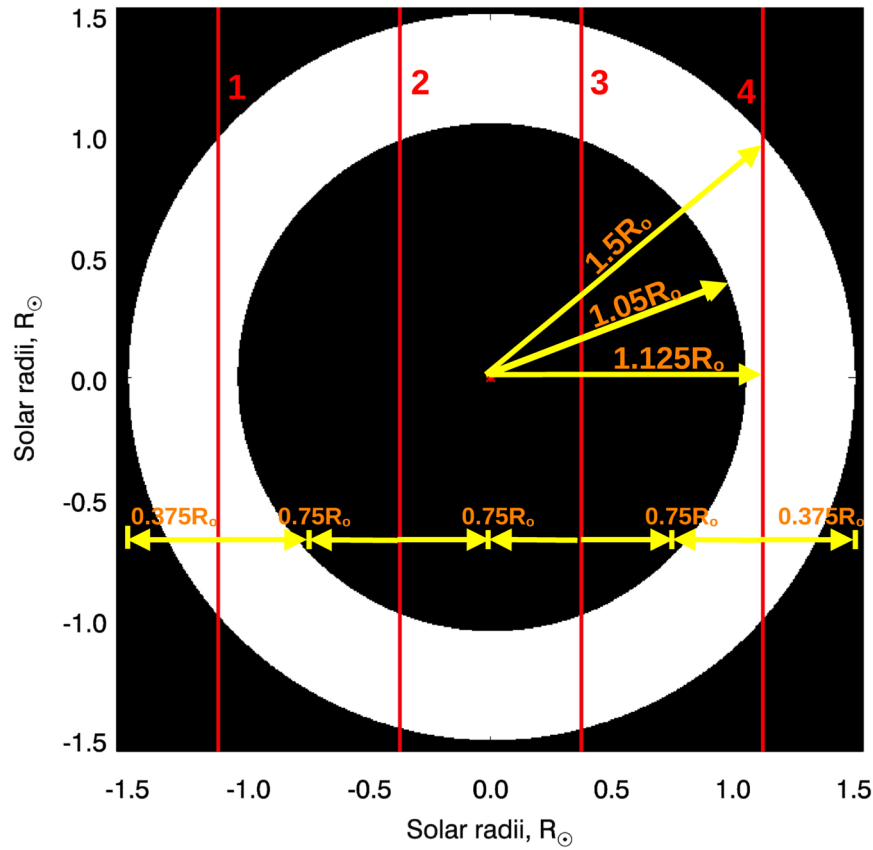
Figure 2. Schematic of the "home" positions of the four slits in the VELC spectroscopy channel. The inner filled black circle corresponds to the occulter (radius $= 1.05\ R_{\odot}$). The white circular patch indicates the FOV, i.e., 1.05–$1.5\ R_{\odot}$. Solar north and east directions are straight up and to the left, respectively.

Table 1
Instrument Parameters Related to VELC Spectral Observations

Parameter	Specifications
Detector pixel size (μm)	6.5
Spatial scale (pixel^{-1})	$1''25$
Slit width (μm)	50 (equivalent to $9''6$)
Slit length (mm)	15 (equivalent to $48'$)
FOV (total) ($R_{\odot}$)	1.05–1.5
FOV (each slit position) ($R_{\odot}$)	$\pm1.5 \times 0.01$ (spatial direction $\times$ dispersion direction)
Separation between slits (mm)	3.75

Table 2
Parameters of the 5303 Å Emission Line Observations on 2024 July 16

Parameter	Specifications
Spectral dispersion (mÅ pixel^{-1})	28
FWHM of the narrowband filter (Å)	6.5
Sit and stare mode	...
Location of center of slit 4 w.r.t to image ($R_{\odot}$)	$r = 1.05$ at west limb
Spatial binning (pixels)	2
Spectral binning (pixels)	1
Exposure time (s)	5 for each spectrum
Cadence (s)	51s
Observation duration (hr)	10 (12:30–22:30 UT)
Raster scan mode	...
FOV($R_{\odot}$)	1.05–1.5 (for all directions)
Step size of LSM (μm)	20 (image movement on slits = 40)
Number of steps	95
Exposure time (s)	5
Number of spectra binned onboard	6 (effective exposure time = 30 s)
Time interval between successive positions of LSM (s)	30
Duration of one raster scan (minutes)	≈47

There was a sudden reduction in the intensity (coronal dimming) at $\approx$13:18 UT around position angle $\approx$265°. The dimming lasted for $\approx$6 hr. It was closely associated with a 1B Hα flare from AR13738 located at heliographic coordinates S06W85 in the interval $\approx$13:18–14:04 UT with maximum at 13:20 UT. The position angle of the above active region is $\approx$264°. This is in good agreement with the position angle of the dimming mentioned above. Note that the exact onset time of the Hα flare is uncertain due to limited available data.[1] Therefore, the start time of the flare could have been before 13:18 UT. Figure 4 shows running difference images of the solar corona generated using observations in 195 Å with Extreme-UltraViolet Imager (EUVI) of the Sun Earth Connection Coronal and Heliospheric Investigation (R. A. Howard et al. 2008) onboard

the Solar Terrestrial Relationship Observatory-A (STEREO-A) around the same time. STEREO-A was at $\approx$E19° during the above epoch.[2] Therefore, the abovementioned location of AR13738 corresponds to $\approx$24° inside the limb in the Earthward direction for STEREO-A view. The flare could be noticed as a

[1] https://www.solarmonitor.org/data/2024/07/16/meta/noaa_events_raw_20240716.txt

[2] https://stereo-ssc.nascom.nasa.gov/cgi-bin/make_where_gif
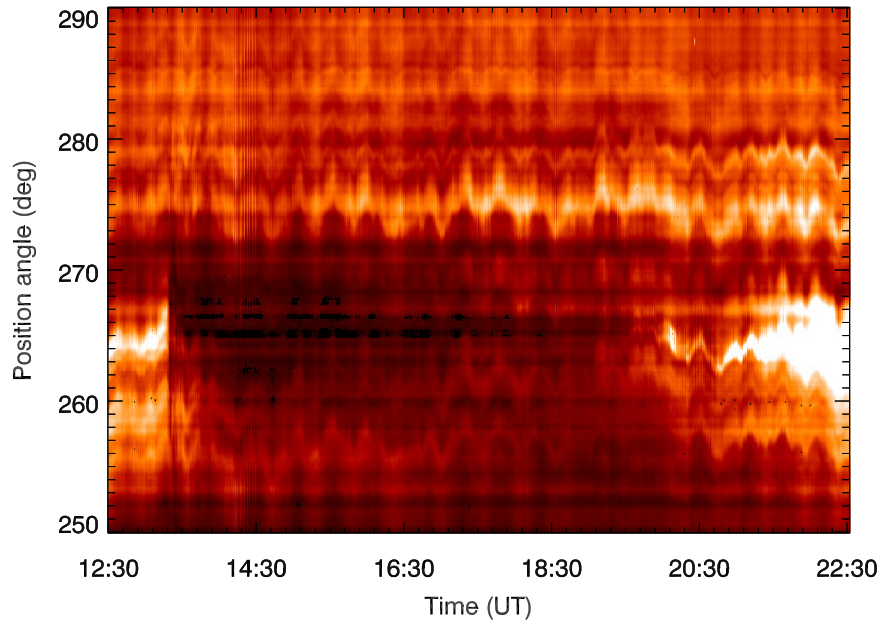
Figure 3. Temporal variations in the peak intensities of the 5303 Å emission line from the solar corona in the position angle range $\approx 250°–290°$ observed on 2024 July 16 with VELC/ADITYA-L1. The center of spectrograph slit 4 was positioned close to the west limb of the Sun at $r \approx 1.05\ R_\odot$. A sudden dimming of the intensity can be clearly observed in the position angle range $\approx 260°–270°$ during the interval $\approx 13:18–19:00$ UT. The possible reasons for the oscillatory pattern in the image are being investigated.
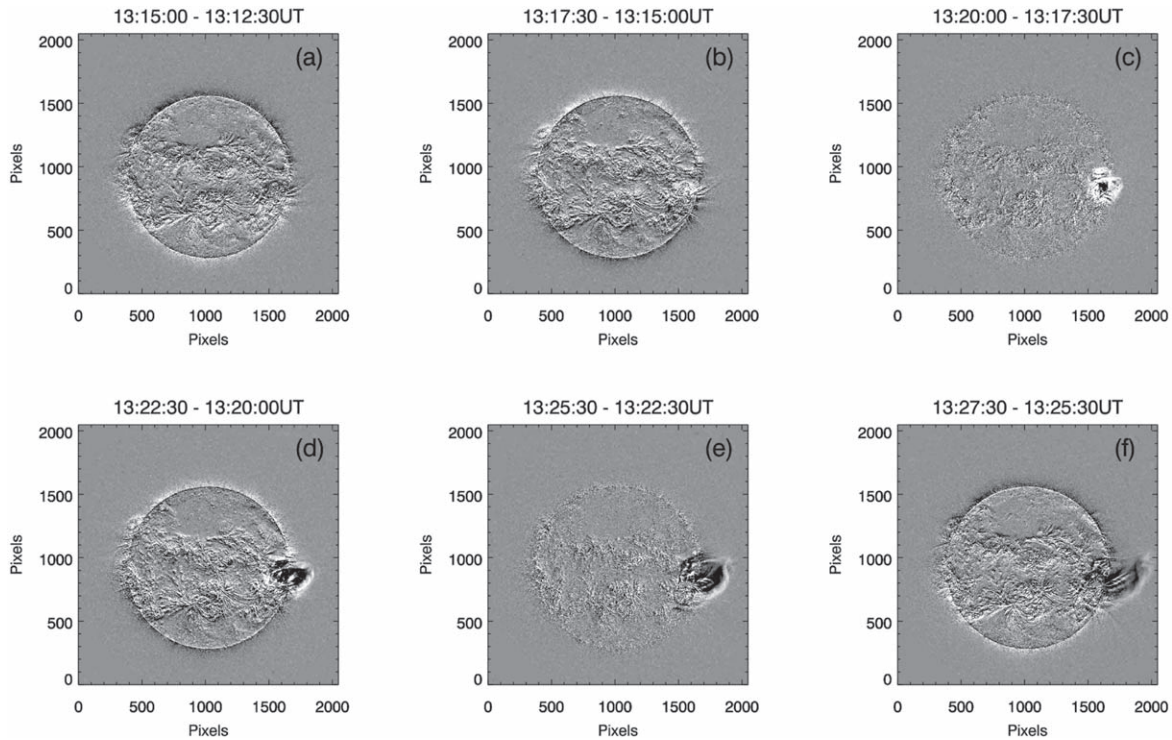

Figure 4. STEREO-A/EUVI 195 Å running difference images for the flare event of 2024 July 16 mentioned in the main text. The observing times of the images used are mentioned above each panel.

brightening near pixel coordinates (1600, 800) in the panel (b) image of Figure 4. This panel indicates that the flare onset was during the interval 13:15:00–13:17:30 UT. The subsequent running difference images indicate an equatorward deflection (in the plane of sky) of the ejected coronal plasma. There was also an X1.9 soft X-ray flare during the interval $\approx 13:11–13:36$ UT with maximum at 13:26 UT in the Geostationary Operational

Environmental Satellite observations. AR13738 was very active on 2024 July 16. There were C5.0 and C4.8 flares at $\approx 12:57$ and $\approx 17:42$ UT, respectively. The comparatively enhanced brightness near the position angle $\approx 265°$ in Figure 3, before and after the dimming event, is likely because of the abovementioned flares. Note that intensity increases due to density enhancements in the solar atmosphere will appear as horizontal bright bands in the
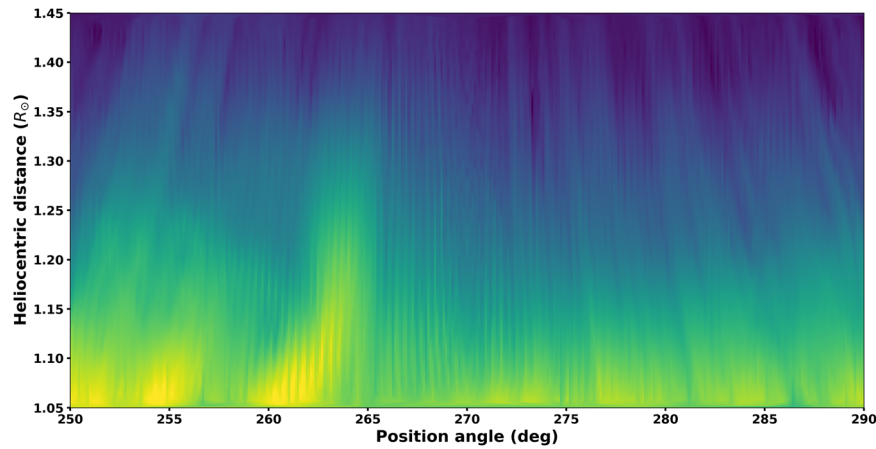
Figure 5. (r, θ) image of the solar corona at the west limb of the Sun constructed from the raster scan observations in the 5303 Å emission line on 2024 July 16 during the interval ≈00:30–01:17 UT, with VELC/ADITYA-L1. The fine lines seen in the image are due to remnant fixed pattern noise in the detector, even after the flat-field correction.
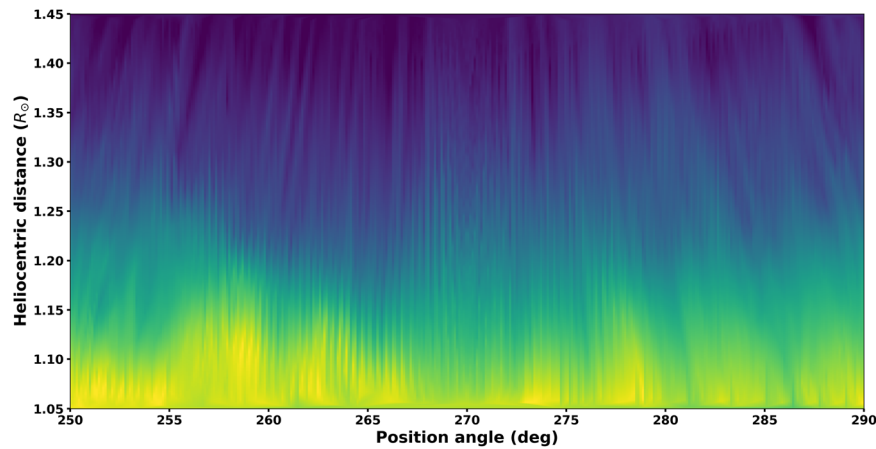
Figure 6. The same as Figure 5, but during the interval ≈23:09–23:56 UT.

5303 Å emission line intensity spectra (see, e.g., K. Hori et al. 2005).

A type II radio burst was reported in the frequency range ≈ 180–25 MHz on 2024 July 16. Its onset time at 180 MHz was ≈13:21 UT. SOHO/LASCO-C2 observed a CME centered at position angle ≈273° with angular width ≈92° close to the flare location mentioned in the previous paragraph.[3] The position angle of the CME is in good agreement with that of the dimming in Figure 3. The first height–time (h–t) measurement of the CME was at ≈14:24 UT when its leading edge was at $r \approx 4.25\,R_\odot$. The second order (quadratic) fit to the h–t measurements of the CME in the SOHO/LASCO FOV indicates that its onset time at $r = 1\,R_\odot$ is ≈13:48 UT. The corresponding time based on linear fit is ≈12:36 UT. The estimated linear speed of the CME in the plane of sky is ≈393 km s^{-1}. Its acceleration in the SOHO-LASCO FOV is ≈ -80.4 m s^{-2}.

We also generated two intensity images of the west limb region of the Sun in the 5303 Å emission line using the raster scan data obtained with slit 4 on 2024 July 16. These were before and after the sit-and-stare observations in Figure 3. The parameters related to raster scan observations mentioned in this work are listed in Table 2. Figure 5 shows the intensity image

in (r, θ) coordinates generated from the raster scan data obtained with slit 4 during the interval ≈00:30–01:17 UT. This time interval is prior to the onset of the CME described above. Coronal structures extending from the edge of the occulter at $r = 1.05\,R_\odot$ until $r \approx 1.50\,R_\odot$ could be seen in the position angle range ≈260°–265°. Figure 6 shows a similar map generated from the raster scan data obtained with slit 4 during the interval ≈23:09–23:56 UT. This time interval is after the CME described above. The coronal structures have changed and reduced in size in the post-CME image (Figure 6) as compared to the pre-CME image ((Figure 5). Considering this, and the close position angle correspondence between the abovementioned coronal loop structures and the CME, we believe that the former are part of the CME that erupted. According to the SOHO/LASCO-C2 CME catalog, there were other CMEs from nearly the same position angle range on 2024 July 16. But the Hα and soft X-ray flares that accompanied this particular CME were very intense as per flare classification. Furthermore, the source region of the flare was almost at the solar limb close to which the spectrograph slit 4 was positioned.

4. Results and Discussions

The upper panel in Figure 7 shows the time variation of 5303 Å emission line intensity at the dimming region (position

---

[3] http://spaceweather.gmu.edu/seeds/ql_lasco/2024/07/20240716.142407.w092.v0393.p273.txt
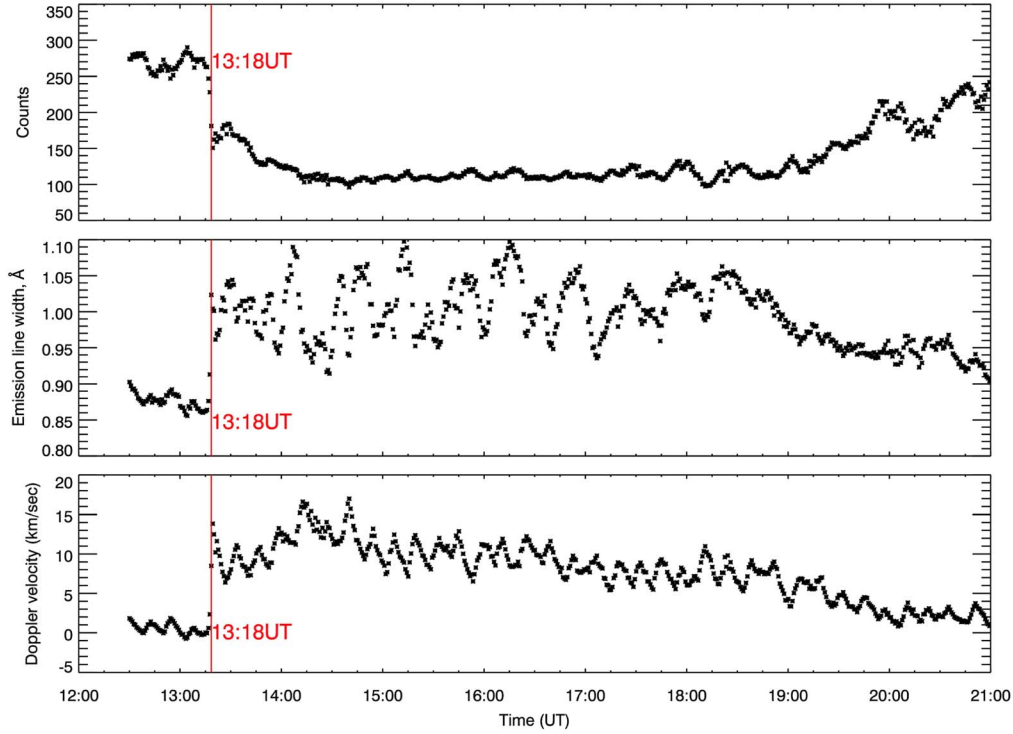
Figure 7. Upper panel: time variation of the peak intensity of the emission line averaged over the dimming region (position angle range ≈260°–270°) in Figure 3. The vertical red line indicates the onset of the dimming at ≈13:18 UT. Middle panel: the same as above, but corresponds to width of the emission line. Lower panel: the same as above, but corresponds to Doppler velocity estimated from the shift in the peak of the emission line from the reference.

angle range ≈ 260°–270°) in Figure 3. The coronal regions observed by slit 4 in the above position angle range are $r \approx 1.07$–$1.05 \, R_\odot$ due to the straight nature of the slit. These distances are smaller than $r \approx 1.2 \, R_\odot$ up to which collisional excitation mechanism is believed to dominate in the line formation (see, e.g., M. Waldmeier 1975; J. Singh 1985; K. P. Raju et al. 1991). Therefore, we assumed that 5303 Å emission line intensity is proportional to square of the electron density n_e. The intensity reduction in Figure 7 is ≈50%. Therefore, the corresponding density decrease should have been ≈7%. Assuming $n_e \approx 1.03 \times 10^9 \, \text{cm}^{-3}$ at $r = 1.05 \, R_\odot$ in the active region corona (B. Vršnak et al. 2004), we find that the above 7% decrease in density corresponds to ≈$7 \times 10^7 \, \text{cm}^{-3}$. Note that this reduction in n_e suggests that radiative excitation may be equally important in the line formation in the present case. But the background n_e is still high ($\sim 10^9 \, \text{cm}^{-3}$) despite the decrease. The ratio of radiative to collisional excitation is expected to be minimal for such large n_e (see, e.g., S. R. Habbal et al. 2007). So our assumption of collisional excitation as the dominant mechanism of 5303 Å line formation in the present case remains good. The above-mentioned decrease in density agrees reasonably with similar values reported due to CME-related coronal dimmings observed in X-rays and radio (A. C. Sterling & H. S. Hudson 1997; N. Gopalswamy & Y. Hanaoka 1998; R. Ramesh & C. V. Sastry 2000; R. Ramesh & E. Ebenezer 2001). The type II radio burst mentioned in Section 3 was first observed near 180 MHz at ≈13:21 UT. The 180 MHz plasma level in the active region corona is expected to be at $r \approx 1.14 \, R_\odot$. The type II radio bursts are widely believed to be magnetohydrodynamic shocks driven by the leading edge of the associated CMEs (see, e.g., R. Ramesh et al. 2012; A. Kumari et al. 2019). Assuming the same, we estimated the possible location of the leading

edge of the CME during the onset of the coronal dimming at 13:18 UT. As per reports, the shock speed estimated from the type II radio burst observations on 2024 July 16 is ≈398 km s^{-1}. This implies that in the interval between the onset time of the coronal dimming (≈13:18 UT) and that of the type II burst (i.e., ≈ 13:21 UT), the CME should have propagated a distance of ≈ 0.1 $R_\odot$. In other words the leading edge of the CME should have been at $r \approx 1.04 \, R_\odot$ at 13:18 UT. There is close agreement between these numbers and that of the coronal dimming (i.e., $r \approx 1.05$–$1.07 \, R_\odot$ at ≈13:18 UT). The position angles of the CME (≈273°) and that of the dimming (≈265°) are also nearly the same. These are in support of our above argument that the dimming observed in the present case is due to CME-induced depletion of coronal material. The duration of the dimming (≈6 hr) is in the range of timescales over which the corona restructures in the aftermath of a CME (see, e.g., C. Kathiravan et al. 2007).

The middle panel in Figure 7 shows the variations in the 5303 Å emission line width (Δw) with time, after correcting for instrumental line profile. The Doppler temperature, T_d (comprising both thermal and nonthermal components) was estimated from the emission line width using the relation, $T_d = \frac{mc^2}{2k_B}\left(\frac{\Delta w}{\lambda}\right)^2$. Here, $m = 9.33 \times 10^{-26}$ kg is the Fe XIV ion mass, and λ is the rest wavelength (5303 Å) of the emission line. The mean emission line widths before and after the onset of the dimming were ≈0.87 and ≈1 Å, respectively. The width has increased by ≈15% during the dimming. Substituting these values in the above relation, we find that T_d increased from ≈ 2.7×10^6 to ≈ 3.6×10^6 K at 13:18 UT. Assuming the thermal component for the Fe XIV ion, the nonthermal velocity (turbulent) was calculated using the relation

$$\left[\left(\frac{\Delta w}{\lambda}\right)^2 \frac{c^2}{4\ln(2)} - \left(\frac{2k_{\mathrm{B}}T}{m}\right)\right]^{1/2}$$ as $\approx 24.87\,\mathrm{km\,s^{-1}}$ for $\Delta w = 1.0$ Å. We assumed $T = 1.8 \times 10^6$ K for the above calculations. Enhanced turbulence because of restructuring of the coronal magnetic field and hence small-scale magnetic reconnections at the source region of the CME, after its lift-off, is a likely reason for the nonthermal line broadening in the present case.

The lower panel in Figure 7 shows the variations in Doppler velocity $\left(\frac{\Delta\lambda}{\lambda}c\right)$. The differences between the peak locations of the emission line profiles and the reference pixel location were computed for each spatial location along the slit, and for the entire observing duration. $\Delta\lambda$ was obtained from the above difference by multiplying it with the spectral dispersion per pixel. The mean Doppler velocity (averaged along the line-of-sight direction) is $\approx 10\,\mathrm{km\,s^{-1}}$ during the dimming. The positive value (redshift) indicates that the associated plasma motions in the ambient corona are directed away from the observing direction. Note that the position angle of the CME source region (i.e., AR13738; see Section 3) is $\approx 264°$. This is different from the central position angle ($\approx 273°$) of the CME mentioned previously. The above difference indicates a possible deflection of the CME by the ambient magnetic field (see, e.g., J. Wang et al. 2020). This could be a likely cause of the abovementioned redshift in the Doppler velocity though the CME originated on the Earthward side of the solar limb. The STEREO-A/EUVI observations shown in Figure 4 are consistent with the above argument related to deflection of the CME.

5. Conclusions

We have reported the first spectroscopic observations of the onset phase of a CME in the 5303 Å coronal emission line with the VELC payload onboard ADITYA-L1. Analysis of the peak intensity of the emission line indicate coronal dimming ($\approx 50\%$) in the aftermath of the CME onset. The dimming was due to depletion of coronal material because of the CME, and lasted for ≈ 6 hr. During the same interval, there was $\approx 15\%$ enhancement in the width of the emission line. The nonthermal velocity (turbulence) during the CME is $\approx 24.87\,\mathrm{km\,s^{-1}}$. Doppler shift calculations using the locations of the emission line peak during the corresponding period indicate a redshift of $\approx 10\,\mathrm{km\,s^{-1}}$. Similar near-Sun observations with VELC/ADITYA-L1 and the UCoMP[4] can help to understand the source regions of the CMEs, particularly using the data on changes in the line width and Doppler shift, the primary characteristics in the spectroscopic observations of CMEs (H. Tian et al. 2013). Such data can help to constrain the parameters used in the modeling of CMEs. The CME event of 2024 July 16 (associated with an X1.9 class flare) described in this work was observed ≈ 1 hr before it appeared in the FOV of SOHO/LASCO-C2. The planned synoptic observations with VELC/ADITYA-L1 would be very useful to constrain the onset time of the CMEs.

Acknowledgments

ORCID iDs

R. Ramesh ⬥ https://orcid.org/0000-0003-2651-0204
V. Muthu Priyal ⬥ https://orcid.org/0000-0001-6093-3302
Jagdev Singh ⬥ https://orcid.org/0000-0003-0562-2979
K. Sasikumar Raja ⬥ https://orcid.org/0000-0002-1192-1804

References

Alzate, N., Habbal, S., Druckmüller, M., Emmanouilidis, C., & Morgan, H. 2017, ApJ, 848, 84
Bagala, L. G., Stenborg, G., Schwenn, R., & Haerendel, G. 2001, JGR, 106, 25239
Boe, B., Habbal, S., Druckmüller, M., et al. 2020, ApJ, 888, 100
Brueckner, G. E., Howard, R. A., Koomen, M. J., et al. 1995, SoPh, 162, 357
Bruzek, A., & Demastus, H. L. 1970, SoPh, 12, 447
Caspi, A., Seaton, D. B., Tsang, C. C. C., et al. 2020, ApJ, 702, 131
Demastus, H. L., Wagner, W. J., & Robinson, R. D. 1973, SoPh, 31, 449
Dere, K. P., Brueckner, G. E., Howard, R. A., et al. 1997, SoPh, 175, 601
Evans, J. W. 1957, PASP, 69, 421
Gopalswamy, N., & Hanaoka, Y. 1998, ApJ, 498, L179
Guhathakurta, M., Fisher, R. R., & Altrock, R. C. 1993, ApJ, 414, L145
Habbal, S. R., Morgan, H., Johnson, J., et al. 2007, ApJ, 663, 598
Hori, K., Ichimoto, K., Sakurai, T., Sano, I., & Nishino, Y. 2005, ApJ, 618, 1001
Howard, R. A., Moses, J. D., Vourlidas, A., et al. 2008, SSRv, 136, 67
Ichimoto, K., Hara, H., Takeda, A., et al. 1995a, ApJ, 445, 978
Ichimoto, K., Ohtani, H., Ishigaki, T., Maemura, H., & Noguchi, M. 1995b, PASJ, 47, 383
Inhester, B., & Schwenn, R. 1997, in Correlated Phenomena at the Sun, in the Heliosphere and in Geospace, ESA SP-415, ed. A. Wilson (Noordwijk: ESA), 47
Kathiravan, C., Ramesh, R., & Nataraj, H. S. 2007, ApJ, 656, L37
Koutchmy, S., Zhugzhda, I. D., & Locans, V. 1983, A&A, 120, 185
Kumari, A., Ramesh, R., Kathiravan, C., Wang, T. J., & Gopalswamy, N. 2019, ApJ, 881, 24
Landi, E., Habbal, S. R., & Tomczyk, S. 2016, JGRA, 121, 8237
Mierla, M., Schwenn, R., Teriaca, L., Stenborg, G., & Podlipnik, B. 2008, A&A, 480, 509
Minarovjech, M., Rušin, V., Rybanský, M., Sakurai, T., & Ichimoto, K. 2003, SoPh, 213, 269
Mishra, S., Sasikumar Raja, K., Sanal Krishnan, V. U., et al. 2024, ExA, 57, 7
Muro, G. D., Gunn, M., Fearn, S., Fearn, T., & Morgan, H. 2023, SoPh, 298, 75
Orrall, F. Q., & Smith, H. J. 1961, AJ, 66, 293
Priyal, M., Singh, J., Prasad, B. R., et al. 2024, AdSpR, 74, 547
Pasachoff, J. M., Babcock, B. A., Russell, K. D., & Seaton, D. B. 2002, SoPh, 207, 241
Pasachoff, J. M., Rušin, V., Druckmüller, M., et al. 2009, ApJ, 702, 1297
Plunkett, S. P., Brueckner, G. E., Dere, K. P., et al. 1997, SoPh, 175, 699
Prasad, B. R., Banerjee, D., Singh, J., et al. 2017, CSci, 113, 613
Prasad, B. R., Suresh Venkata, N., Natarajan, V., et al. 2023, JATIS, 9, 044001
Raj Kumar, N., Raghavendra Prasad, B., Singh, J., & Venkata, S. 2018, ExA, 45, 219
Raju, K. P., Desai, J. N., Chandrasekhar, T., & Ashok, N. M. 1991, JApA, 12, 311
Ramesh, R., Anna Lakshmi, M., Kathiravan, C., Gopalswamy, N., & Umapathy, S. 2012, ApJ, 752, 107
Ramesh, R., & Ebenezer, E. 2001, ApJL, 558, L141
Ramesh, R., & Sastry, C. V. 2000, A&A, 358, 749
Rušin, V., Rybanský, M., Minarovjech, M., & Pinter, T. 1994, in IAU Symp. 154, Infrared Solar Physics, ed. D. M. Rabin, J. T. Jefferies, & C. Lindsey (Cambridge: Cambridge Univ. Press), 211
Sakurai, T. 1998, in ASP Conf. Ser. 140, Synoptic Solar Physics, ed. K. S. Balasubramaniam, J. Harvey, & J. Rabin (San Francisco, CA: ASP), 483
Schwenn, R., Inhester, B., Plunkett, S. P., et al. 1997, SoPh, 175, 667

---

[4] https://www2.hao.ucar.edu/mlso/instruments/upgraded-coronal-multi-channel-polarimeter

Singh, J. 1985, SoPh, 95, 253

Singh, J., Hasan, S. S., Gupta, G. R., Nagaraju, K., & Banerjee, D. 2011a, SoPh, 270, 213

Singh, J., Ichimoto, K., Imai, H., Sakurai, T., & Takeda, A. 1999, PASJ, 51, 269

Singh, J., Prasad, B. R., Suresh Venkata, N., & Amit, K. 2019, AdSpR, 64, 1455

Singh, J., Prasad, B. R., Venkatakrishnan, P., et al. 2011b, CSci, 100, 167

Singh, J., Ramesh, R., Prasad, B. R., et al. 2024, SoPh, submitted

Singh, J., Sakurai, T., Ichimoto, K., & Watanabe, T. 2004, ApJ, 617, L81

Sterling, A. C., & Hudson, H. S. 1997, ApJ, 491, L55

Suresh Venkata, N., & Prasad, B. R. 2021, OptEn, 60, 074103

Suzuki, I., Sakurai, T., & Ichimoto, K. 2006, PASJ, 58, 165

Sykora, J. 1992, SoPh, 140, 379

Tian, H., Tomczyk, S., McIntosh, S. W., et al. 2013, SoPh, 288, 637

Tsubaki, T. 1975, SoPh, 43, 147

Venkata, S. N., Prasad, B. R., Nalla, R. K., & Singh, J. 2017, JATIS, 3, 014002

Voulgaris, A. G., Gaintatzis, P. S., Seiradakis, J. S., Pasachoff, J. M., & Economou, T. E. 2012, SoPh, 278, 187

Vršnak, B., Magdalenić, J., & Zlobec, P. 2004, A&A, 413, 753

Waldmeier, M. 1975, SoPh, 45, 147

Wang, J., Hoeksema, J. T., & Liu, S. 2020, JGRA, 125, e27530